

Table 1

Chemical composition of high purity boehmite used for preparation of alumina supports.

Chemical composition ^a (wt%)								
Sample	Al ₂ O ₃	SiO ₂	Fe ₂ O ₃	CaO	MgO	Na ₂ O	K ₂ O	Heavy metals
Boehmite	99.95	0.012	0.010	0.005	0.005	0.002	0.002	0.010

^a Data from the manufacturer.

level with a diesel containing 240 ppmw S was obtained. Similar effects of nickel loading and particle size on desulfurization of a commercial diesel fuel with 240 ppmw of sulfur have been reported by Ko et al. [11] for SBA-15-supported nickel adsorbent. Shalaby et al. [6] studied the desulfurization performance of various nickel-based adsorbents supported on MCM-48, SBA-15, and SiO₂–Al₂O₃ in a fixed-bed flow adsorption system at 493 K and found that nickel loading, particle size, and also type of support had strong effects on the adsorptive performance of the adsorbents. They also found that the desulfurization selectivity was remarkably dependent on the number and size of the alkyl groups especially at the 4- and 6-positions in alkyl DBTs.

To the best of our knowledge, there is no report on reduced nickel-based sulfur adsorbents supported on different phases of alumina as opposed to several studies published on silica- and silica–alumina-supported nickel adsorbents [2,6,10–12]. Transitional aluminas, particularly γ -Al₂O₃, δ -Al₂O₃, and θ -Al₂O₃, which are usually obtained by calcination of boehmite (γ -AlOOH) at different temperatures, are among the most important oxides used in the industrial applications [13]. The aluminas are widely used as adsorbents, catalysts, and catalysts supports, due to their large specific surface areas, well-defined pore size distributions, stability within a wide temperature range, ability to stabilize and disperse the active phases as well as moderate acidities. There are several reports representing key roles of alumina polymorphs as catalysts supports [14–19]. Laurenti et al. [20] reported that different polymorphs of alumina in alumina-supported CoMo catalysts resulted in different turnover frequencies (TOF) in HDS of 4,6-DMDBT. This was attributed to different interactions between support and the active phase. Chary et al. [21] evaluated nickel catalysts supported on pure and mixed polymorphs of alumina for hydrodechlorination of chlorobenzene and found that a mixture of (γ + θ) had the best catalytic performance which was attributed to the higher dispersion of NiO nanoparticles on this support. Rashkeev et al. [22] reported that Cr/ η -Al₂O₃ catalytic system lasted up to 3 years without any degradation, whereas Cr/ γ -Al₂O₃ degraded within a few weeks in dehydrogenation of alkanes. Since nickel-based sulfur adsorbents lose their activities during adsorption step and need to be regenerated periodically, probably via high temperature oxidation and subsequent reduction treatments, durability of the adsorbents becomes a key feature for their industrial application. The considerable effects of the phase of the alumina supports on various catalytic systems has motivated us to investigate the behavior of nickel adsorbents supported on various phases of alumina for reactive adsorption of DBT and 4,6-DMDBT.

Thus, the principal objective of the present work was to study the physicochemical properties of different nickel adsorbents supported on γ -Al₂O₃, δ -Al₂O₃, and θ -Al₂O₃ and explore the possible relation between the RADS of the adsorbents with structure of the alumina supports. The RADS activity of the adsorbents were compared for removing DBT and 4,6-DMDBT from a simulated diesel fuel made of DBT or 4,6-DMDBT (250 ppmw S) in hexadecane at 473 K and atmospheric pressure. The synthesized adsorbents were characterized by inductively coupled plasma (ICP) atomic emission spectroscopy, X-ray diffraction (XRD), Fourier transform infrared (FTIR) spectroscopy, N₂ adsorption–desorption, ammonia temperature-programmed desorption (NH₃-TPD), hydrogen

temperature-programmed reduction (H₂-TPR), scanning electron microscopy (SEM), and high resolution transmission electron microscopy (HR-TEM).

2. Experimental

2.1. Chemicals

All chemicals were used as received without further purification. High purity boehmite (AlOOH, 1.8 mm spheres, 99.95%) was a commercial product from Sasol. Nickel (II) nitrate hexahydrate (Ni(NO₃)₂·6H₂O, \geq 99%), *n*-hexadecane (*n*-C₁₆, \geq 99%), and dibenzothiophene (DBT, \geq 98%) were purchased from Merck. 4,6-Dimethylbenzothiophene (4,6-DMDBT, 95%) was obtained from Acros.

2.2. Preparation of alumina supports

The alumina supports were prepared from Sasol high purity boehmite spheres (1.8 mm) to rule out the side effects of impurities on desulfurization performance of the adsorbents. Elemental analysis of high purity boehmite is listed in Table 1. The boehmite spheres were calcined at 873, 1173, and 1273 K for 6 h in static air (heating rate 3 K/min). Subsequently, the samples were allowed to cool down to room temperature by natural cooling. XRD and FTIR spectroscopy were carried out for each sample to verify the complete transformation of the boehmite to the desired alumina phase. The as-prepared alumina samples were used for preparation of supported nickel adsorbents without further treatment.

2.3. Preparation of alumina-supported nickel adsorbents

The supported nickel adsorbents were prepared by a modified incipient wetness impregnation (IWI) of the alumina supports. Due to large differences between surface areas of the supports, 5.0 atoms of nickel per nm²_{support} were loaded on each support to obtain the same surface density of nickel atoms (see Table 2). The proper amount of Ni(NO₃)₂·6H₂O was dissolved in deionized water, and the solutions were then added into the support materials. Subsequently, the impregnated supports were ultrasonicated in a BANDELIN-Model DT 255H ultrasonic bath for 4 h in order to achieve uniform distribution of nickel atoms on surfaces of the supports. The adsorbent samples were then dried in an oven at 323 K overnight, crushed and sieved to mesh size of 140–230 (particle size 63–100 μ m). Finally, the adsorbents were dried at 323 K for another 48 h and stored in a dessicator for adsorption experiments. The synthesized samples were labeled x Ni/ γ -alumina, x Ni/ δ -alumina, and x Ni/ θ -alumina, where x represents weight percent of metallic nickel on the basis of plain supports.

2.4. Characterization of adsorbents

XRD patterns of the supports and adsorbents were acquired on a X'Pert Philips Diffractometer with Cu K α radiation (λ = 1.54056 \AA) in a step scanning mode over 2 θ angle between 10° and 80° at a

Table 2

Preparation conditions, nickel particle size and adsorption performance of adsorbents.

Adsorbent ^a	Ni content ^b (wt%)	Ni surface density (atom/nm ² _{Support})	D ^c (nm)	d _{VA} ^d (nm)	d _{XRD} ^e (nm)	D ^f (%)	TOF _{DBT} ^g (h ⁻¹)	TOF _{4,6-MDBT} ^g (h ⁻¹)
10.2Ni/γ-alumina	9.25	5.0	2.5	4.5	5.2	22	110	89
7.6Ni/δ-alumina	7.11	5.0	2.2	4.0	3.6	25	114	90
5.4Ni/θ-alumina	5.13	5.0	2.1	3.9	3.7	26	112	88

^a Concentrations of impregnation solutions for preparation of 10.2Ni/γ-alumina, 7.6Ni/δ-alumina, and 5.4Ni/θ-alumina were 2.34, 2.25, and 1.74 (mol_{Ni}/L), respectively.^b g Ni/(g Ni + g Al₂O₃) × 100.^c Mean diameter of Ni particles estimated by TEM ($d = \sum n_i d_i / \sum n_i$).^d Volume–area mean diameter of Ni particles estimated by TEM ($d_{VA} = \sum n_i d_i^3 / \sum n_i d_i^2$).^e Nickel crystallite size estimated from Scherrer formula ($L = K\lambda / (\beta \cos \theta)$, $K = 0.9$, $\lambda = 1.54056 \text{ \AA}$).^f Nickel dispersion calculated by Eq. (2) on the assumption of spherical particles.^g Initial rates of DBT or 4,6-MDBT removal per surface Ni⁰ atom. (Surface Ni⁰ atom = $D \times \text{total Ni atoms} \times \text{reduced fraction}/100$).

scan speed of 1.5°/min. Different alumina phases were identified by comparing the more intense peaks at specific 2θ angles.

FTIR spectra of the supports were recorded on a Bruker Vector 22 spectrometer equipped with a DTGS detector. The spectrometer was used in transmission mode with a resolution of 5 cm⁻¹ in the range of 400–4000 cm⁻¹. The samples for IR measurements were prepared as pellets by embedding the alumina particles in a KBr matrix with an alumina:KBr ratio of 2:100. A background spectrum was collected before collection of the samples' spectra. The spectrum of each sample was corrected for the background.

The specific surface areas and pore size distributions of the supports and nickel adsorbents were measured by analysis of nitrogen isotherms collected at 77 K using a Micromeritics ASAP 2010 apparatus. Prior to the measurements, the samples (0.1 g) were outgassed at 573 K for 2 h under vacuum. The surface areas were calculated from the N₂ adsorption at relative pressures of 0.05 < P/P_0 < 0.3 by Brunauer–Emmett–Teller (BET) equation. The pore size distributions were determined by Barrett–Joyner–Halenda (BJH) method from adsorption branch of the N₂ physisorption isotherms.

The alumina-supported nickel adsorbents were dissolved in aqua regia and the elemental analysis of Ni content in the samples were performed using ICP-AES.

NH₃-TPD from the three alumina supports was conducted using a Quantachrome CHEMBET-3000 apparatus equipped with a thermal conductivity detector (TCD). In order to evaluate acidities of the samples, adsorption of anhydrous ammonia was carried out at 323 K by exposing 0.15 g of the samples to 20 sccm 5.0 vol% NH₃/He gas mixture for 1.5 h. After purging the materials of physically adsorbed NH₃ at 323 K, ammonia TPD was performed at a heating rate of 10 K/min from 323 up to 1000 K under pure He.

H₂-TPR was carried out to assess the reducibility of the nickel precursor on the different alumina supports. About 50 mg of each adsorbent was loaded into a U-shaped quartz reactor and heated up to 1100 K in a flow of 7.0 vol% H₂/Ar gas mixture at a heating rate of 10 K/min. The consumption of H₂ was monitored with a TCD.

SEM images were obtained on an FEI NOVA 200 NANOLAB microscope operated at 15–17.5 kV. The samples were mounted on a copper holder and coated with a thin layer of gold to avoid charging effect. HR-TEM analyses were performed using a JEOL EM-2010F instrument operating at accelerating voltage of 200 kV. The samples were ultrasonically dispersed in ethanol and the obtained suspensions were deposited on a carbon-coated copper grid.

2.5. Reactive adsorption of DBT and 4,6-DMDBT

Evaluation of RADS performance of the different alumina supports and the alumina-supported nickel adsorbents was conducted in a 50-ml three-neck glass batch reactor equipped with a magnetic stirrer, a condenser, sampling line, and a temperature controller as described in our previous study [23]. Prior to RADS tests, 0.5 g of the dried sample was loaded into a tubular quartz reactor and reduced

at 873 K for 4 h (heating rate 3 K/min) under an upward flow of high purity hydrogen gas (20 sccm). After reduction was completed, the hydrogen gas stream leaving the reduction reactor was passed through the batch reactor in order to purge the reactor from oxygen. When the temperature of the adsorbent bed was decreased to 473 K, the reduced adsorbent was quickly introduced into the batch reactor containing 10 mL of a simulated diesel fuel. The model fuels were prepared by dissolving the appropriate amount of DBT or 4,6-DMDBT (250 ppmw S) in proper amount of n-C₁₆. The RADS progress was monitored by taking samples from the reactor at different times, i.e., after 10 s, 30 s, 1, 2, 5, 10, 30, 60, 120, and 180 min. The sulfur concentration of the samples was measured by injecting 1 μL of the samples into a gas chromatograph (GC) purchased from Teif-Gostar company equipped with DB-1 capillary column (30 m long × 0.25 mm I.D. × 1 μm film thickness) and a flame photometric detector (FPD). The injector was used in splitless mode and ultra-high purity helium was used as the carrier gas with a flow rate of 1 mL/min. The GC-FPD instrument was calibrated with standard solutions of DBT and 4,6-DMDBT in n-C₁₆ considering the nonlinear response proposed by Ma et al. [10]. The temperature of GC oven was programmed as follows: holding at 453 K for 1 min, raising from 453 to 563 K with a ramp rate of 10 K/min, and finally holding at 563 K for 1 min.

2.6. Temperature-programmed oxidation (TPO)

The spent 10.2Ni/γ-alumina was further characterized by TPO. The spent adsorbent was thoroughly washed (three times) with pure n-hexane and dried at 343 K. About 0.1 g of the sample was loaded in a tubular quartz reactor and heated up to 1173 K under a flow of air (10 sccm) by increasing the temperature at a ramp rate of 10 K/min. The effluent gases exiting the TPO reactor were passed through a gas cell and infrared spectra of evolved SO₂, CO₂, and CO were instantaneously recorded on a Bruker Vector 22 FTIR spectrometer.

3. Results and discussion

3.1. Characterization of supports and adsorbents

3.1.1. X-ray diffraction (XRD)

Fig. S1 shows the temperatures at which different alumina phases were formed. The boehmite (AlOOH) was transformed to γ-, δ-, and θ-alumina phases at 873, 1173, and 1273 K, respectively. The XRD patterns for the alumina phases are presented in Fig. 1a,c,e. The alumina phases, i.e., γ-alumina (JCPDS Card No. 43-1308), δ-alumina (JCPDS Card No. 46-1131), and θ-alumina (JCPDS Card No. 35-0121) were identified based on the highest intensities shown by miller indices in the figure. Diffraction patterns for the alumina-supported nickel adsorbents reduced at 873 K for 4 h and passivated in 1.0 vol% O₂/He gas mixture (10 sccm) at room temperature for 2 h (Fig. 1b,d,f), displayed broad peaks for metallic nickel

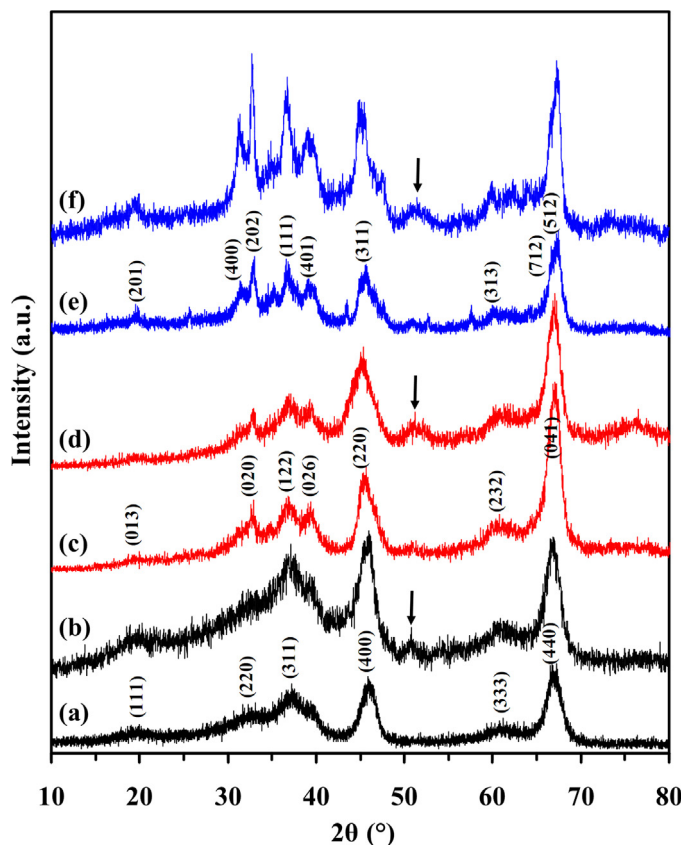


Fig. 1. XRD patterns for (a) γ -alumina, (b) 10.2Ni/ γ -alumina, (c) δ -alumina, (d) 7.6Ni/ δ -alumina, (e) θ -alumina, and (f) 5.4Ni/ θ -alumina.

marked by arrows. As shown in Table 2, the crystallite size of the nickel estimated according to the XRD patterns decreased when the calcination temperature of the alumina support was raised. It has been reported in the literature that direct reduction of nickel nitrate leads to the formation of smaller nickel metal particles [24]. Calcination prior to reduction leads to the formation and aggregation of large metal particles, owing to the partial decomposition of the nickel-support mixed oxides and formation of larger oxide particles during the calcination [24].

3.1.2. Fourier transform infrared (FTIR) spectroscopy

The alumina phases evolution was further confirmed by FTIR measurements, the results of which are presented in Fig. 2. The IR spectrum of γ -alumina presented a wide pattern with two unresolved bands extending from 450 to 950 cm^{-1} . This pattern is typical of a complex crystallographic structure [13]. For the samples prepared at higher calcination temperatures, the spectra displayed better resolved and more intense peaks between 450 and 950 cm^{-1} . For the alumina phase prepared at 1173 K, several sharp peaks appeared which could be assigned to δ -alumina. As the calcination temperature further increased to 1273 K, the IR bands turned out to be more well-defined and the bands at 565, 628, 760, and 826 cm^{-1} clearly confirmed the existence of θ -alumina [13,25]. The peaks at 565 and 628 cm^{-1} correspond to AlO_6 stretching modes, whereas, those at 760 and 826 cm^{-1} can be assigned to AlO_4 stretching modes.

3.1.3. N_2 adsorption–desorption

BET Surface areas, total pore volumes, and average pore diameters for all alumina phases are listed in Table 3. Upon heating the boehmite from 873 to 1273 K, the surface area and pore volume decreased by 47 and 28%, respectively. This may be attributed to

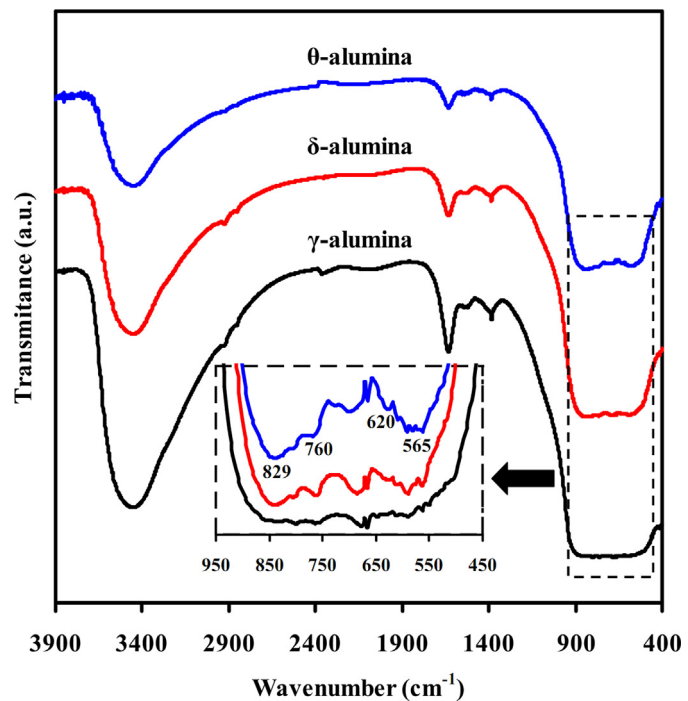


Fig. 2. FTIR spectra of the different alumina phases prepared from boehmite.

Table 3
Results of BET surface area, pore volume, and BJH pore diameter of alumina supports and alumina-supported nickel adsorbents.

Sample	Surface area (m^2/g)	Pore volume (ml/g)	Pore diameter ^b (nm)
γ -Alumina	209	0.74	10.0
10.2Ni/ γ -alumina ^a	192	0.62	9.0
δ -Alumina	157	0.58	14.3
7.6Ni/ δ -alumina ^a	146	0.48	13.6
θ -Alumina	111	0.53	18.4
5.4Ni/ θ -alumina ^a	103	0.44	17.9

^a Supported nickel adsorbents were reduced at 873 K for 4 h and passivated in 1 vol% O_2/He gas mixture prior to N_2 adsorption–desorption measurements.

^b Pore diameters were calculated based on adsorption branch of N_2 adsorption–desorption isotherms.

the thermal sintering and change in crystalline structure of the alumina from γ to δ to θ . However, the average pore diameter increased from 10 to 18.4 nm from γ -alumina to θ -alumina. For all of the supports, no micropore volume could be measured by the *t*-plot method indicating that only mesopores were developed for all of the alumina phases. The data concerning porosity characteristics of alumina-supported nickel adsorbents are summarized in Table 3 and in Fig. 3. In all cases, the nitrogen adsorption–desorption isotherms correspond to the type-IV with H1 hysteresis loop (cylindrical pores) according to the IUPAC classification. The inset image of Fig. 3 shows nearly monomodal pore size distributions with maximum frequencies of pore diameters at 9.0, 13.6, and 17.9 nm for 10.2Ni/ γ -alumina, 7.6Ni/ δ -alumina, and 5.4Ni/ θ -alumina, respectively. The decrease in the average pore diameter following nickel loading showed that most of the pores were still available and little pore blockage, if present, occurred due to the nickel nitrate impregnation and its subsequent reduction, an indication of good dispersion of nickel species on all alumina surfaces.

3.1.4. Temperature-programmed desorption of ammonia (NH_3 -TPD)

TPD of adsorbed ammonia was conducted on different alumina phases to compare the amount and the strength of the surface acid

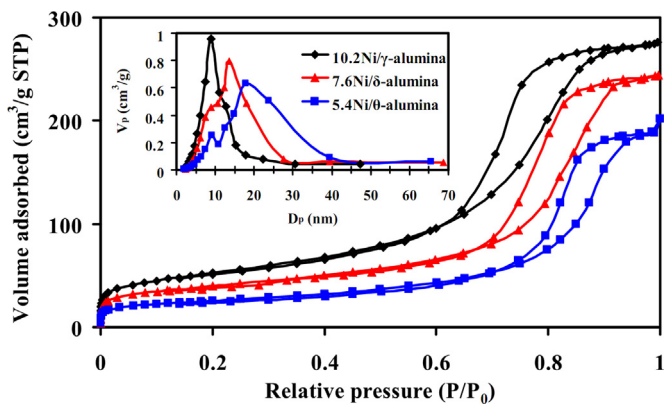


Fig. 3. N_2 adsorption–desorption isotherms and corresponding pore size distribution for the alumina-supported nickel adsorbents.

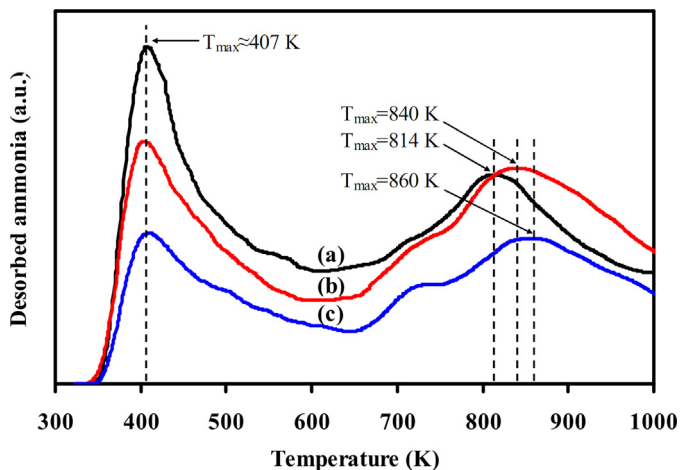


Fig. 4. NH_3 -TPD profiles of (a) γ -alumina, (b) δ -alumina, and (c) θ -alumina prepared from boehmite.

sites of these materials. The area under the NH_3 -TPD profile represents the total amount of acid sites, while the temperatures of the peaks are indicative of the strength of the acidic sites. The NH_3 -TPD profiles of the alumina phases are shown in Fig. 4a–c and the results are summarized in Table 4. The peaks were classified and attributed to the acid sites with different strengths, i.e., weak plus medium and strong, according to the temperatures of their maxima. The first desorption peak between 350 and 615 K was assigned to the weak and moderate strength acid sites, whereas, the second peak between 615 and 1000 K was corresponded to the strong acid sites [26,27]. For the γ -alumina obtained by calcination of boehmite at 873 K, there were two peaks at 407 and 814 K (Fig. 4a), while the second peak was shifted to higher temperatures with increasing the calcination temperature, i.e., 840 and 860 K for δ -alumina and θ -alumina (Figs. 4b,c), respectively. The intensity of the desorption peaks gradually decreased with the increase of calcination temperature, suggesting less acidic sites were present in the samples. Increasing the heat treatment temperature to 1173 K increased the total density of the acid sites by 24% of that for γ -alumina. However,

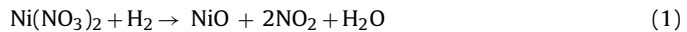
only 15% increase in total density of the acid sites was observed upon calcination at 1273 K. The decline in the acid site density for θ -alumina compared to δ -alumina can be ascribed to the surface reconstruction [28]. The density of strong acid sites increased by 40% and 32% for δ -alumina and θ -alumina, respectively, compared to that of γ -alumina. This may be attributed to greater density of low coordination surface aluminum ions in δ - and θ -alumina due to more surface dehydroxylation. It is most likely that only strong acid sites contributed to sulfur adsorption at the high temperature of 473 K.

Surprisingly, the influence of the alumina support acidity on the nickel dispersion under reducing atmosphere has scarcely been reported in the literature [29]. Lif et al. [29] studied sintering of nickel particles supported on different phases of alumina in an ammonia+hydrogen atmosphere. They found that sintering may be correlated to the number of low coordination surface aluminum sites (strong acid sites). These strong acid (oxidizing) sites increased the metal-support interaction, through withdrawing electrons from the nickel atoms [30], which in turn suppressed diffusion and agglomeration of nickel particles/atoms. Interestingly, we observed for the adsorbents of this study that nickel supported on δ - and θ -alumina showed higher resistance towards sintering than nickel supported on γ -alumina (Table 2). In analogy with the results reported by Lif et al., we hypothesized that nickel interacted strongly with strong acid sites of alumina supports. δ - and θ -alumina had higher ratios of strong acid site densities to surface loading of nickel, compared to the γ -alumina. Therefore, nickel particles supported on the former alumina phases, were more stable against sintering than the nickel particles supported on latter one.

3.1.5. H_2 -temperature-programmed reduction (H_2 -TPR)

The reducibility of the nickel species are usually considered as an indication of strength of its interaction with alumina supports [31]. Therefore, any differences in TPR profiles could be interpreted as changes in the interaction between the nickel moieties and the supports.

The TPR profiles of the impregnated alumina phases, performed without any previous calcination, are presented in Fig. 5a–c which illustrates different steps of reduction. Degree of reduction of the adsorbents is defined as the ratio of H_2 consumption, quantified by integrating the areas of the second and the third peaks obtained by deconvolution of the TPR profiles, to the theoretical H_2 consumption. The relation between H_2 consumption and the peak area was calibrated by injecting accurately known amount of H_2 into the empty quartz cell under the same testing conditions. In the TPR spectra of alumina-supported $\text{Ni}(\text{NO}_3)_2$, a sharp H_2 consumption peak was present at around 610 K. The signal had area of 0.65, 0.78, and 0.74 equivalents of H_2 to Ni for 10.2Ni/ γ -alumina, 7.6Ni/ δ -alumina, and 5.4Ni/ θ -alumina, respectively, which may be attributed to the decomposition of the nitrate anion according to Eq. (1).



The amount of consumed H_2 was less than stoichiometric, owing probably to the formation of basic nickel nitrate, i.e., $\text{Ni}(\text{NO}_3)_2 \cdot 2\text{Ni}(\text{OH})_2$, during sonication, drying, and initial step of

Table 4
Acidic properties of the alumina supports determined by NH_3 -TPD.

Support	Acidity ($\mu\text{mol NH}_3/\text{g}_{\text{support}}$)			Acid density (NH_3 molecule/ $\text{nm}^2_{\text{support}}$)		
	Weak + medium	Strong	Total	Weak + medium	Strong	Total
γ -Alumina	277.9	340.2	618.1	0.80 (45%)	0.98 (55%)	1.78
δ -Alumina	216.0	358.6	574.5	0.82 (37%)	1.37 (63%)	2.20
θ -Alumina	140.5	237.9	378.4	0.76 (37%)	1.29 (63%)	2.05

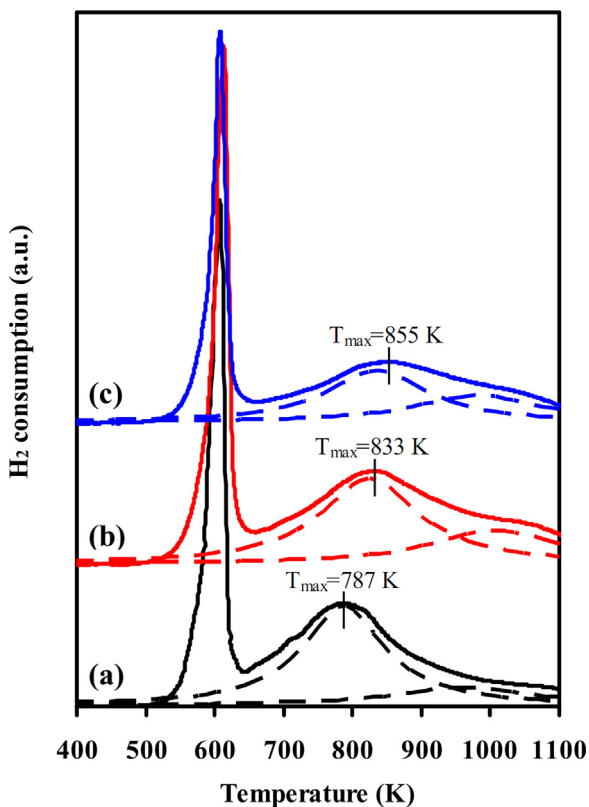


Fig. 5. TPR profiles of impregnated (a) 10.2Ni/γ-alumina, (b) 7.6Ni/δ-alumina, and (c) 5.4Ni/θ-alumina adsorbents without any previous calcination.

TPR [24,32]. At a higher temperature, a broad signal of H_2 consumption was observed. The area for this peak corresponds to the reduction of highly dispersed surface NiO particles interacting strongly with the support and more diffuse oxide phases, such as Ni-rich and Al-rich mixed oxides and nickel spinels ($NiAl_2O_4$) [19,33–35]. As it is shown in Table 5, for the samples 7.6Ni/δ-alumina and 5.4Ni/θ-alumina, the total area of the second and the third H_2 consumption peaks corresponded to the stoichiometric value ($H_2/Ni = 1$). This result showed that all of the Ni species in these adsorbents were reduced to the metallic state. On the other hand, for the sample 10.2Ni/γ-alumina, the H_2 consumption was slightly lower ($H_2/Ni = 0.9$). This shows that approximately 10% of nickel species in 10.2Ni/γ-alumina adsorbent were not in reduced (Ni^0) state and nickel ions were incorporated deep in the γ-alumina lattice as a solid solution and became hard-to-reduce species [35]. Based on density functional calculations, Rashkeev et al. [22] reported that it was energetically favorable for some transition metals to occupy a subsurface layer position in $\gamma-Al_2O_3$ and $\eta-Al_2O_3$. However, the activation barrier for the transition metal

to enter such position in $\gamma-Al_2O_3$ was much lower than that for $\eta-Al_2O_3$. This may explain the lower H_2/Ni ratio observed for nickel supported on γ-alumina compared to the δ- and θ-alumina. The crystalline structure of δ- and θ-phases can retard the trapping of Ni ions in the subsurface layers of these supports which enhances the Ni dispersion on their surfaces.

By comparing the TPR profiles, it is evident that the crystalline/textural properties of alumina supports affect the reduction of impregnated nickel nitrate and the second reduction peak temperature followed the order: 5.4Ni/θ-alumina > 7.6Ni/δ-alumina > 10.2Ni/γ-alumina. This is a clear indication of a weaker interaction between the nickel species and the γ-alumina support compared to the δ- and θ-alumina. Roman et al. [36] reported that the high degree of dispersion of supported nickel oxide may make nucleation more difficult and inhibit the propagation of the reduction reaction boundaries. As a consequence, the peaks at 833 K and 855 K might be assigned to the reduction of NiO particles smaller than those reducible at 787 K. Our results are in good agreement with those obtained by Chary et al. [21]. Louis et al. [24] studied the reduction of Ni/SiO₂ system prepared by impregnation of SiO₂ with nickel nitrate without any calcination step. They observed the formation of nickel phyllosilicates during drying, storage, and TPR of the impregnated sample which was attributed to a condensation reaction of OH groups of the basic nickel nitrate with those of silica surface. Before complete reduction, the nickel phyllosilicates were probably located at the interface of silica and the remaining nickel, for which they acted as anchoring sites.

It is believed that the third deconvolution peak, shown in Fig. 5, could be due to the reduction of surface Ni–Al mixed oxide phases [31,37,38]. As it is shown in Table 5, the percentage of the overall nickel content as surface Ni–Al mixed oxide phases (including spinel) in the adsorbents increased with calcination temperature of the supports and followed the order: 10.2Ni/γ-alumina < 7.6Ni/δ-alumina < 5.4Ni/θ-alumina. From our results on alumina-supported nickel adsorbents, it may be concluded that the size of nickel metal particles is determined by the amount of surface nickel species strongly interacting with the support, i.e., Ni–Al mixed oxides. These species act as anchoring sites for weakly interacting nickel. Since the proportion of Ni–Al mixed oxides was greater for nickel adsorbents on the support calcined at higher temperatures, the metal particles tend to be smaller for these adsorbents. During TPR at 873 K nickel particles can undergo sintering due to the reduction of the Ni–Al mixed oxides followed by weakening of their anchoring strength and also to Ni^0 migration induced by thermal effect.

3.1.6. Scanning and high resolution transmission electron microscopy (SEM and HR-TEM)

SEM and HR-TEM images of the reduced and passivated 10.2Ni/γ-alumina and 5.4Ni/θ-alumina adsorbents are displayed in Fig. 6A–D. Nickel particles could hardly be observed on both alumina supports in SEM images. As confirmed by XRD analyses, nickel crystallites were very small (3.6–5.2 nm). Therefore, the reduced nickel could not be observed with such a low resolution SEM which only presents the macroporous structure of the alumina phases.

HR-TEM analysis was carried out to investigate the size distribution and average size of the nickel particles. Fig. 6C,D show that all samples exhibited finely dispersed nickel particles and some aggregated particles. Lattice fringes (insets of Fig. 6C,D) could clearly be recognized and the fringe spacing was measured to be ca. 0.2 nm corresponding to d-spacing of Ni (111) plane. Compared to 10.2Ni/γ-alumina, 7.6Ni/δ-alumina (not shown), and 5.4Ni/θ-alumina adsorbents showed less aggregated particles, indicating that the latter alumina phases were preferred for obtaining higher nickel dispersion, which was in agreement with the NH₃-TPD and H₂-TPR results. The volume-area mean particle size of the nickel agglomerates in 10.2Ni/γ-alumina, 7.6Ni/δ-alumina, and 5.4Ni/θ-

Table 5
TPR characteristics of impregnated Ni/alumina adsorbents.

Adsorbent	H_2/Ni^a (peak 1)	H_2/Ni^b (peak 2)	Area 3/(area 2 + area 3) ^c (%)
10.2Ni/γ-alumina	0.65	0.9	24
7.6Ni/δ-alumina	0.78	1.2	34
5.4Ni/θ-alumina	0.74	1.0	40

^a (mol H_2 consumed in TPR during decomposition of nitrate)/(mol Ni_{total}).

^b (mol H_2 consumed in TPR after decomposition of nitrate)/(mol Ni_{total}) = degree of reduction. The amount of hydrogen consumption was quantified by integrating and calibrating area of the second deconvolution peak of TPR profile obtained by reduction of the sample up to 873 K and holding at 873 K for 4 h.

^c Proportion of overall Ni content as Ni–Al mixed oxide phases (including spinel).

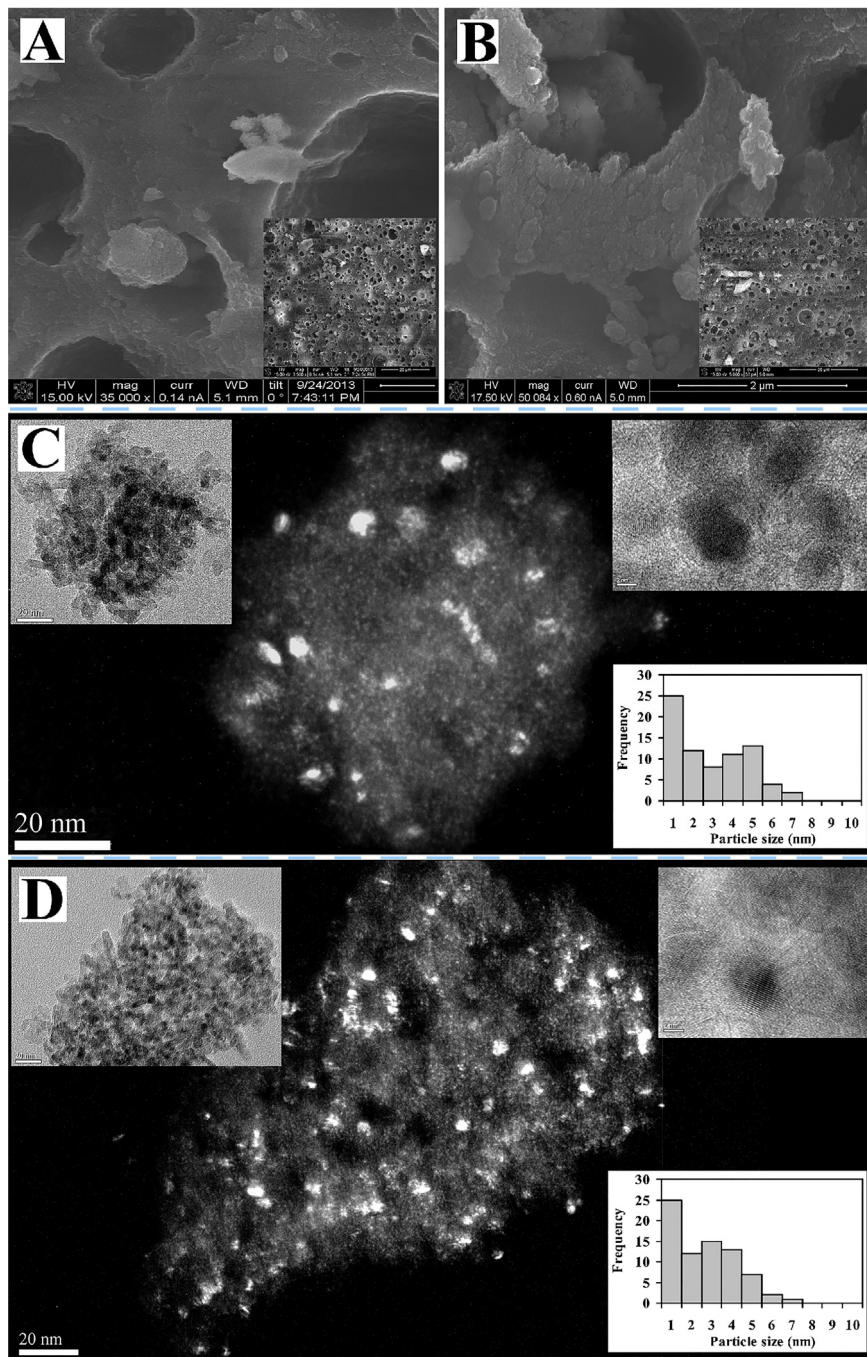


Fig. 6. SEM images of (A) 10.2Ni/γ-alumina and (B) 5.4Ni/θ-alumina. TEM images of (C) 10.2Ni/γ-alumina and (D) 5.4Ni/θ-alumina.

alumina samples were determined to be ca. 4.5, 4.0, and 3.9 nm, respectively. Therefore, it is plausible that such small particles can scarcely be detected with low resolution SEM analyses. The dispersion (D) of nickel particles can be estimated using the volume-area mean diameter (d_{VA}) of nickel particles measured by TEM according to Eq. (2) (see Table 2).

$$D = 6(\nu_{Ni}/a_{Ni})/d_{VA} \quad (2)$$

where, ν_{Ni} and a_{Ni} are the volume occupied by a nickel atom in the bulk of metal (10.95 \AA^3) and the area occupied by a surface nickel atom (6.51 \AA^2), respectively. The number of the surface Ni^0 atoms could be estimated using dispersion, the total number of nickel atoms and the degree of reduction.

3.2. Reactive adsorption of DBT and 4,6-DMDBT

3.2.1. Effect of alumina supports

The desulfurization performance of metal-supported adsorbents strongly depends on the properties of both the metal and the support material. In order to investigate the role of support, desulfurization experiments were carried out using alumina phases as 'blank' adsorbents. The percent DBT/4,6-DMDBT removal is defined as the amount of DBT/4,6-DMDBT eliminated from the model fuel with respect to the initial amount of DBT/4,6-DMDBT multiplied by 100. A comparison between percent sulfur compound removal from model fuels containing 250 ppmw S as DBT or 4,6-DMDBT with different aluminas as 'blank' adsorbents are

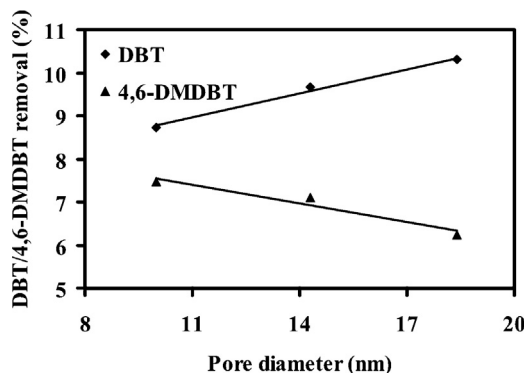


Fig. 7. Overall DBT/4,6-DMDBT removal as a function of average pore diameter of alumina supports.

shown in Figs. S2 and S3a, respectively. Insets show the sulfur removal at short adsorption times. It can be seen from Fig. S2a that removal of DBT followed the order: θ -alumina > δ -alumina > γ -alumina. The amount of 4,6-DMDBT removal was less than that for DBT which followed the order: γ -alumina > δ -alumina > θ -alumina. This decline in the desulfurization performance of alumina supports for 4,6-DMDBT compared to DBT suggests that direct active site-sulfur atom interaction contributes to the adsorption of these sulfur compounds over alumina phases. In case of active site- π electron interaction, a higher 4,6-DMDBT removal should be expected since the methyl groups in 4,6-DMDBT molecule augment the density of π electrons on the aromatic rings [39]. Adsorption of sulfur compounds onto different alumina phases is a complex process and mainly controlled by both chemical interactions and physical factors. The DBT family of sulfur compounds can display some Lewis base character due to the lone electron pairs on the sulfur atom. Therefore, they can be adsorbed on the available acid sites of the alumina supports via acid-base interaction [40]. Since the RADS tests were carried out at a high temperature ($T=473$ K) it is most likely that only strong acid sites contribute to sulfur adsorption [41]. However, the present data indicate that no direct relationship could be found between the amount of strong acid sites, Table 4, and the DBT/4,6-DMDBT removal for the alumina supports. This possibly indicates that only a fraction of NH_3 (critical diameter of 3.6\AA)-titrated surface acid sites are accessible to bulky DBT/4,6-DMDBT molecules ($\sim 8\text{\AA}$). It has been reported that pore structure of adsorbents plays important role and influences the desulfurization performance [2,6]. The pore structure affects the diffusion of large aromatic sulfur compounds of fuel between pore mouth and active sites on the interior of the adsorbent particle, where most of active sites are located. Larger pores facilitate higher mass transfer rates for the bulky sulfur compounds. In Fig. 7, the DBT/4,6-DMDBT removal is plotted as a function of the pore size of the supports. There was a linear correlation between the average pore sizes of the alumina supports and the desulfurization performance, for both DBT and 4,6-DMDBT compounds. DBT removal linearly increased with the average pore sizes of the supports. θ -alumina having the lowest surface area demonstrated the highest DBT removal performance followed by δ -alumina. γ -alumina with the highest surface area had the lowest DBT removal. On the contrary, desulfurization performances of the alumina supports for removing 4,6-DMDBT followed the order: γ -alumina > δ -alumina > θ -alumina. Although, diffusion of bulky sulfur compounds into the pore structure of θ -alumina with larger pores was easier compared to the other alumina supports, 4,6-DMDBT molecule due to strong steric hindrance resulting from methyl groups at 4- and 6-positions had weaker interaction with the active sites. This steric hindrance may increase the interaction distance between the S atom and the acid sites, resulting in a weaker interaction. Consequently, only the more

exposed acid sites, such as Lewis acid sites on the edges and corners or single hydroxyl groups which are more abundant on γ -alumina surface compared to δ -alumina and θ -alumina [14] may be able to interact with the sulfur. Larrubia et al. [42] studied the adsorption of DBT and 4,6-DMDBT on alumina by FTIR spectroscopy and reported that, because of the steric hindrance, the adsorption of 4,6-DMDBT on the Lewis acid sites was limited. Nair et al. [43] reported that active centers for sulfur adsorption were primarily acidic single hydroxyl groups which were augmented by a proper calcination treatment. Calcination at higher temperatures may result in loss of these hydroxyl groups from the surface to a large extent, thereby decreasing the desulfurization performance. This can explain the different behaviors of the alumina phases for removal of DBT and 4,6-DMDBT with strong steric hindrance. Therefore, the performances of the supports at operating conditions of this study (473 K, atmospheric pressure) was discerned to be more dependent on the joint effect of pore size and amount of available acid sites for each of the sulfur compounds rather than specific surface area and the pore volume of the adsorbents. When the specific sulfur removal, defined as the amount of sulfur compound removed divided by the surface areas of the alumina supports, is considered (Figs. S2 and S3b), it is observed that the density of adsorbed DBT and 4,6-DMDBT was always higher for θ -alumina and δ -alumina compared to γ -alumina and followed the order: θ -alumina > δ -alumina > γ -alumina. Similar to the overall sulfur removal, this trend may be attributed to the interplay between the available acid site density and the average pore size of the different alumina phases.

3.2.2. Effect of nickel active phase

In order to investigate the effect of nickel loading and potential synergy between nickel and alumina supports on the RADS performance of the adsorbents, further experiments were carried out using 10.2Ni/ γ -alumina, 7.6Ni/ δ -alumina, 5.4Ni/ θ -alumina. All adsorbents with the nickel surface loading of $5.0\text{Ni}_{\text{atom}}/\text{nm}^2$ support, were reduced in H_2 at 873 K for 4 h before use and their RADS performances were evaluated at 1 bar pressure and 473 K under hydrogen atmosphere. The results for desulfurization of DBT and 4,6-DMDBT (250 ppmw S in $n\text{-C}_{16}$) are shown in Figs. 8 and 9, respectively. Two regions of desulfurization may be distinguished for all adsorbents: a remarkable sulfur removal occurred in less than 10 min, followed by a quasi plateau up to 3 h. The overall sulfur removal increased with nickel loading indicating that nickel was a key component interacting directly with the sulfur compounds and followed the order: 10.2Ni/ γ -alumina > 7.6Ni/ δ -alumina > 5.4Ni/ θ -alumina. However, when specific sulfur removal was considered the order was reversed. By using a model fuel (DBT + $n\text{-C}_{16}$) containing 500 ppmw S, better differentiation of the overall and specific sulfur removals associated with different nickel adsorbents was attained and the results are depicted in Figs. S4a,b, respectively. Compared to 10.2Ni/ γ -alumina, 5.4Ni/ θ -alumina and 7.6Ni/ δ -alumina showed $\sim 31\%$ increase in DBT removal, respectively, at short adsorption time ($t=10$ s). Similarly, 26% more 4,6-DMDBT removal were obtained over 5.4Ni/ θ -alumina and 7.6Ni/ δ -alumina than 10.2Ni/ γ -alumina. Only a small portion (<5%) of the observed specific adsorption performances at 10 s of the adsorption test was associated with the supports. This manifested that nickel particles acted as the principal adsorption sites (>95%) for the sulfur compounds and the observed differences in the RADS performances were mainly due to the differences in the extent of available nickel sites. This can be ascribed to the pore structures of alumina phases and size of metallic nickel particles. At short adsorption time that most of the active sites were still available and pore blockage and coke formation were not the issue, larger pore diameters of δ -alumina and θ -alumina resulted in a less pore diffusion limitation, which in turn increased the accessibility of nickel sites and the specific sulfur removal. On the other hand, as it was

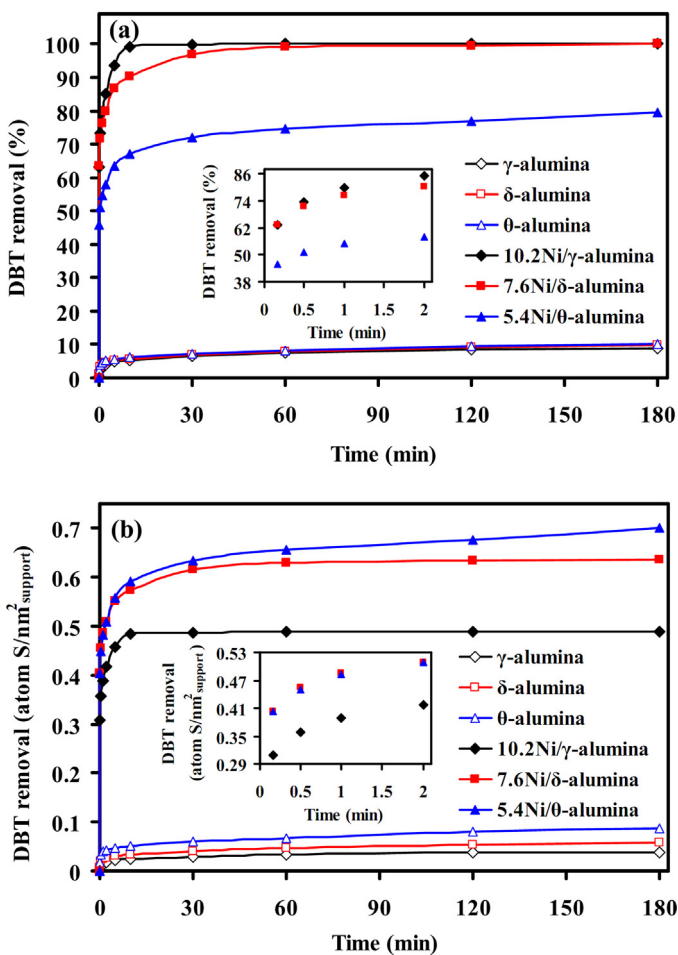


Fig. 8. Comparison of (a) overall DBT removal and (b) specific DBT removal on alumina-supported nickel adsorbents as a function of time. Adsorption condition: 7.7 g of model fuel (250 ppmw S as DBT in *n*-hexadecane), 473 K and atmospheric pressure of H₂.

discussed in Section 3.1.5, higher degrees of reduction and smaller nickel particle sizes were found for θ -alumina and δ -alumina supports. Therefore, more specific sulfur removal, even in the absence of diffusion limitations, was expected. Using the number of surface nickel atoms obtained from TEM analysis, degree of reduction, and the initial rates, the TOF per surface Ni⁰ atom was estimated for DBT and 4,6-DMDBT removal and the results are listed in Table 2 (for more details, see Supporting information). The TOF per surface Ni⁰ atom did not change significantly suggesting higher specific activity was caused by different nickel dispersion on different alumina phases rather than by an increase in intrinsic activity of the sites.

A comparison of the specific adsorption performance of alumina-supported nickel adsorbents for DBT and 4,6-DMDBT showed that all adsorbents were about 20% less active for removing the latter refractory sulfur compound. This finding is of great importance, especially when both sulfur compounds co-exist in the fuel. Fig. S5 reveals that for a model fuel composed of DBT (125 ppmw S), 4,6-DMDBT (125 ppmw S), and *n*-C₁₆, 7.6Ni/ δ -alumina had higher selectivity for adsorption of DBT than 4,6-DMDBT. DBT may inhibit the adsorption of 4,6-DMDBT on the surface of the adsorbent through a competitive adsorption on the nickel active sites. Since the difference between the two compounds arises from two methyl groups at 4- and 6-positions of 4,6-DMDBT, the lower adsorption activity for this compound suggested that direct interaction between exposed nickel and sulfur atoms had more contribution for the adsorption of this type of sulfur compounds over the

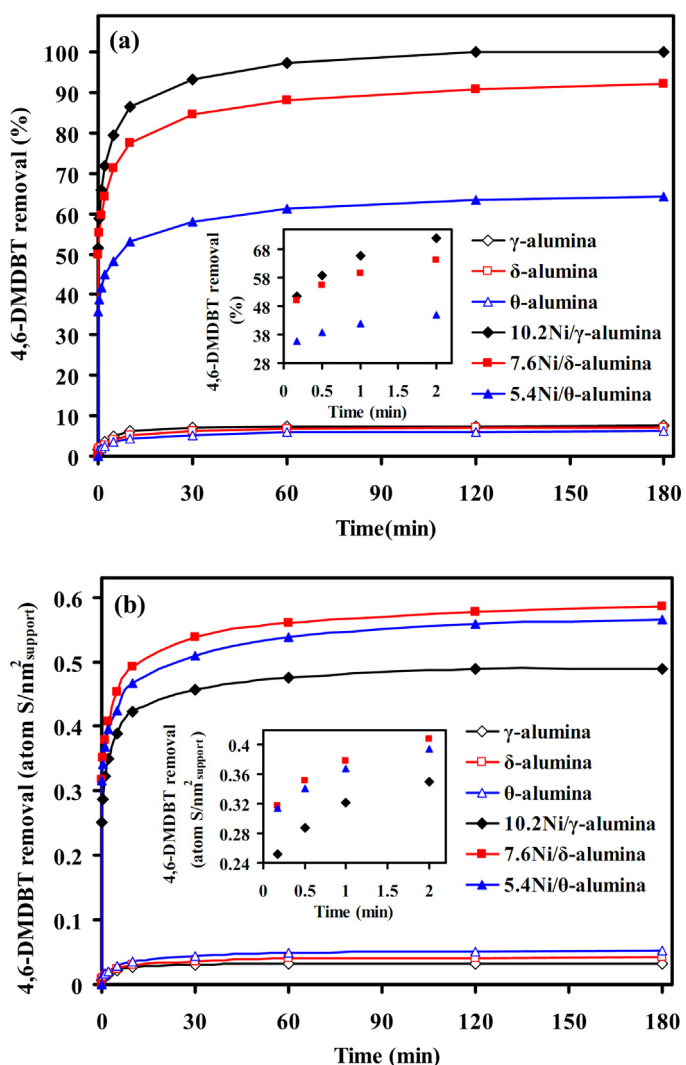


Fig. 9. Comparison of (a) overall 4,6-DMDBT removal and (b) specific 4,6-DMDBT removal on alumina-supported nickel adsorbents as a function of time. Adsorption condition: 7.7 g of model fuel (250 ppmw S as 4,6-DMDBT in *n*-hexadecane), 473 K and atmospheric pressure of H₂.

adsorbents. If Ni⁰– π electron interaction was the preferred type of interaction for adsorption of 4,6-DMDBT, a higher sulfur removal should have been occurred for this compound since the methyl groups in 4,6-DMDBT molecule are electron donor to the aromatic rings and increase the density of π electrons.

Shalaby et al. [6] proposed a mechanism involving a direct coordination between sulfur and nickel atoms on Ni⁰/SiO₂ and reported that methyl groups on the 4- and 6-position of 4,6-DMDBT increased the interaction distance between the S atom and the nickel sites, resulting in a weaker interaction. Accordingly, only the more exposed nickel atoms may be able to interact with the sulfur, resulting in a lower desulfurization performance of the nickel-based adsorbents for the DBTs with strong alkyl steric hindrance. Kim et al. [40] studied the adsorption of 1-methylnaphthalene (1-MNap) on Ni⁰/SiO₂–Al₂O₃ adsorbent and showed that methyl groups on the aromatic ring of naphthalene had almost no effect on the adsorption of naphthalene (Nap) even at room temperature. This further supports our interpretation and is a clear indication of direct reduced nickel-sulfur atom interaction as the preferred adsorption mechanism over our Ni⁰/alumina adsorbents.

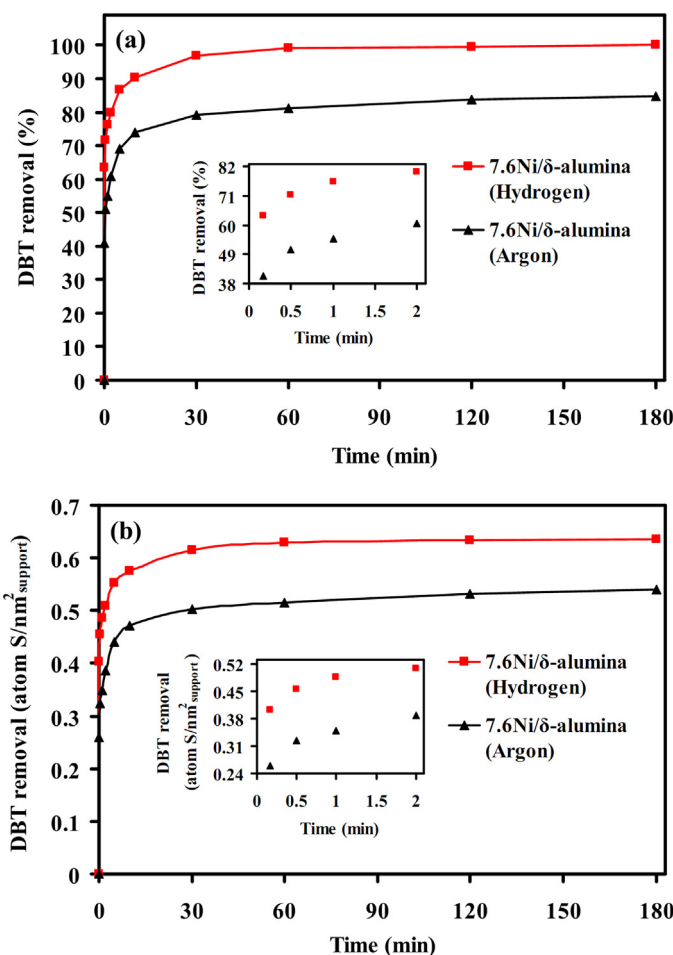


Fig. 10. Dependence of (a) overall DBT removal and (b) specific DBT removal vs. adsorption time on the purging atmosphere. Adsorption condition: 7.7 g of model fuel (250 ppmw S as DBT in *n*-hexadecane), 473 K.

3.2.3. Effect of purging gas

According to our previous study, alumina-supported nickel adsorbent has high adsorptive activity even in the absence of hydrogen as the purging gas [23]. In order to examine effect of the purging atmosphere on the adsorption performance of the alumina-supported nickel adsorbent, adsorption test was performed on 7.6Ni/δ-alumina under identical conditions except that after introducing the reduced adsorbent into the batch reactor the purging gas was switched to Ar from H₂. The results for RADS performance of 7.6Ni/δ-alumina under H₂ and Ar atmospheres are shown in Fig. 10. Again, the two different zones of desulfurization could be distinguished. Under H₂, the activity of 7.6Ni/δ-alumina showed 55% increase in sulfur removal after 10 s. This revealed that the type of purging gas, even at atmospheric pressure, had a strong effect on the sulfur removal efficiency over reduced nickel-based adsorbents. Ma et al. [44] and Huang et al. [45] reported that during desulfurization of thio-phenic compounds on metallic nickel, dissociative chemisorption of sulfur compounds occurred. This may involve hydrogenolysis of C–S bonds to form nickel sulfides and hydrocarbon radicals which were subsequently saturated with chemisorbed hydrogen atoms present on the nickel from the reduction step. From the adsorption theory, it is known that at a fixed temperature and adsorbate concentration, the relative amount of adsorbate on an adsorbent surface depends on the adsorption strength produced by attractive forces between the adsorbate molecules and adsorbent. The coverage of an adsorbent surface by an adsorbate

increases with increasing attractive forces between adsorbate and adsorbent. The order of adsorption strength on nickel surface is: nitrogenated hydrocarbons > oxygenated hydrocarbons > aromatics (including sulfur compounds) > olefins > paraffins [46]. It should be noted that saturated hydrocarbons (paraffins and cycloparaffins) do not adsorb on the nickel surface at temperatures between 366 and 533 K [47,48]. Therefore, when unsaturated hydrocarbons such as aromatic intermediates resulting from sulfur compounds or olefins formed by cracking of the solvent molecules are adsorbed on nickel surface and the surface is heated, the adsorbed molecule rather than being desorbed reversibly decomposes to evolve hydrogen. This leads the surface to be covered by the partially dehydrogenated fragments, i.e., coke precursors.

In the absence of H₂ with appropriate pressure, the RADS activity decreased after a relatively short period of time due to coke formation on the surface of nickel. In addition, *n*-C₁₆ molecules, i.e., solvent, may undergo catalytic cracking over acidic sites of the alumina supports. Coke is the main byproduct of cracking reactions and can block pores of the alumina support which in turn decreases the accessibility of nickel active sites [27]. Thus, a combination of three phenomena may cause two-zone behavior observed for the nickel-based adsorbent: (1) rapid adsorption of sulfur compound on nickel active sites (2) formation of Ni_xS_y surface layer which may be followed by a slower bulk transformation into Ni₃S₂ [49], (3) coke formation on nickel active sites, and (4) pore blockage by coke. Saleh et al. [50] studied sulfidation of nickel by H₂S and observed that the activation energy for sulfidation process progressively increased as the thickness of Ni_xS_y layer increased. Due to high densities of both the reduced nickel and sulfide layer [51], it is plausible to assume that diffusion of the Ni²⁺ or S²⁻ ions through these structures is the rate-determining step [50,51]. FTIR analysis (not shown for the sake of brevity) of the effluent of batch reactor demonstrated that there was no H₂S resulting from Ni_xS_y reduction. Therefore, it is unlikely that the improved performance of the adsorbent in the first zone was due to in situ reduction of the used surface nickel atoms under atmospheric pressure of H₂ and 473 K. Addition of H₂ to the adsorption system may enhance the hydrogenation of the dehydrogenated byproducts adsorbed on the nickel active sites or deposited on surface of the support (via hydrogen spillover) for a short time which consequently frees nickel/support surface and improves the kinetic and capacity of nickel-based adsorbents. Landau et al. [12] reported that in the absence of hydrogen flow, coke formation on nickel surface by radical dimerization and disproportionation may take place. They observed that addition of ethanol, as hydrogen source, at 18 bar and 503 K could suppress coke formation. It is likely that the similar trend observed in the second zone for H₂ and Ar-mediated adsorption tests, was due to low pressure of H₂ which was not able to hydrogenate surface nickel sulfide species and coke precursors effectively for a long time. In order to further clarify whether deactivation by coke (precursors) or sulfur (compound) adsorption on the surface was the main cause of the observed plateau, a RADS test was conducted under the same conditions as Fig. 8 except that it was performed at 373 K to diminish adsorbent deactivation by coke (precursors). The results for overall DBT removal at adsorption temperatures of 373 and 473 K are shown in Fig. S6. The same plateau for sulfur removal at 373 K revealed that the adsorption of sulfur (compounds) on the reduced nickel surface was the primary source of the two-zone behavior observed for the adsorbents.

3.3. Temperature-programmed oxidation (TPO)

Fig. 11 shows the HR-TEM of coke deposited on a nickel particle, FTIR spectrum and the corresponding TPO profiles of the evolved SO₂, CO₂, and CO during temperature-programmed oxidation of spent 10.2Ni/γ-alumina adsorbent. The sample was thoroughly

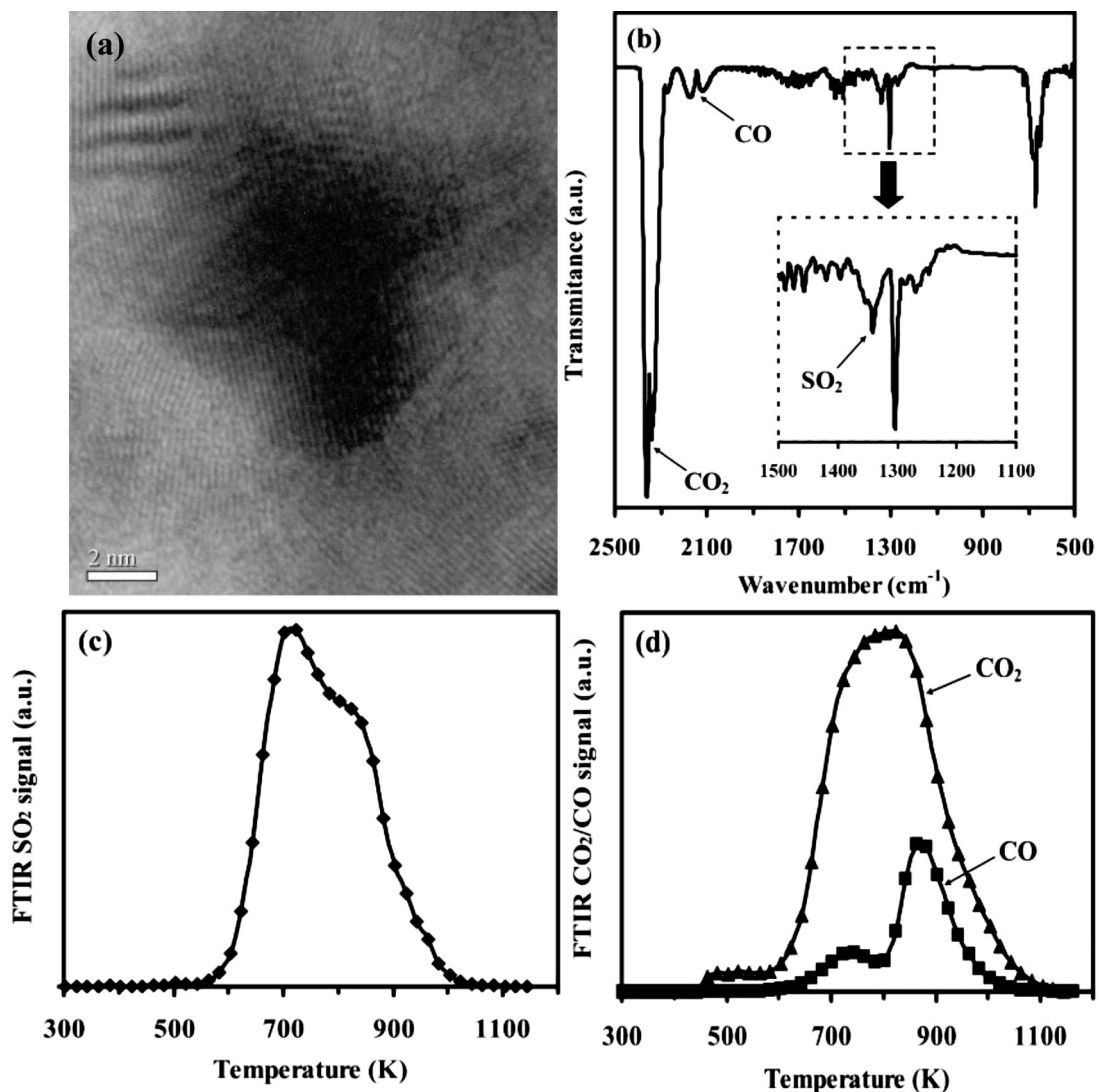


Fig. 11. (a) HR-TEM of coked nickel adsorbent, (b) FTIR spectrum, (c) SO₂, and (d) CO/CO₂ evolutions during TPO of the spent 10.2Ni/γ-alumina adsorbent in air at heating rate of 10 K/min. Adsorption condition: 7.7 g of model fuel (500 ppmw S as DBT in *n*-hexadecane), 473 K, and atmospheric pressure of H₂.

washed with *n*-hexane (three times) and dried at 343 K before use. The peak at ~ 1350 cm⁻¹ corresponds to SO₂ and the bands in the ranges of 2400–2280 cm⁻¹ and 2235–2030 cm⁻¹ are assigned to CO₂ and CO, respectively. The IR spectrum demonstrated the existence of some sulfur and carbon species in the adsorbent which originated from oxidation of Ni_xS_y/DBT and the deposited coke. SO₂ evaluation profile showed a peak at 713 K. Furthermore, this observation showed that a threshold temperature of about 713 K was required to oxidize the adsorbed sulfur species and remove them from the adsorbent surface before it could be reused for the subsequent reduction and adsorption steps. This agrees well with the TPO results reported by Dasgupta et al. [52]. As is seen in Fig. 11, the temperatures associated with maximum CO₂ and CO evolutions were about 823 and 863 K, respectively. This may suggest that even a higher temperature was needed to remove coke from the adsorbent surface. Therefore, the threshold temperature of the oxidative regeneration of the alumina-supported nickel adsorbents should be determined based on both SO₂ and CO_x TPO profiles.

4. Conclusions

The same nickel loading of 5.0Ni atom per nm² on γ-, δ-, and θ-aluminas were prepared and used for reactive

adsorptive desulfurization (RADS) of dibenzothiophene and 4,6-dimethylbenzothiophene at 473 K and atmospheric pressure. The relationship between the physicochemical properties and specific activity of the adsorbents indicated that the RADS performance of the adsorbents was profoundly affected by the pore structure of the support and the interaction between the support and nickel as the active phase. As compared with γ-alumina, the θ- and δ-alumina supported nickel adsorbent showed about 31 and 26% higher specific RADS activity for removing DBT and 4,6-DMDBT, respectively. This was attributed to the higher density of strong acid sites, enhanced reducibility, and dispersion of nickel particles. We may conclude that the stability of alumina-supported nickel against sintering was partly correlated to the acidic nature of the alumina supports. An alumina support with higher density of strong acid sites may improve nickel-support interaction which in turn suppressed the diffusion of nickel particles/atoms on the support surface. Furthermore, θ- and δ-alumina supports augmented nickel dispersion via formation of Ni-Al mixed oxides at the metal-support interface. It was shown that the crystalline structure of δ- and θ-phases, contrary to γ-alumina, could retard trapping of Ni ions in the subsurface layers of these supports which were hard to reduce. Additionally, 4,6-DMDBT showed lower reactivity than DBT that was an indication of the direct interaction between sulfur atom

and nickel active sites as the preferred adsorption mechanism on nickel-based adsorbents. This was attributed to the steric hindrance of methyl groups at 4- and 6-positions of DBT. Moreover, it was found that the type of purging gas (H_2 vs. Ar) could significantly affect the activity of nickel-based adsorbents even at atmospheric pressure. 55% higher RADS activity was observed on Ni/ δ -alumina under H_2 atmosphere than under Ar. TPO-FTIR analysis revealed the existence of sulfur and coke on the surface of spent adsorbent which were believed to be the main causes of adsorbents deactivation.

Acknowledgements

This work was supported by funding from the National Iranian Oil Refining & Products Distribution Company, Catalysis and the Nanostructured Materials Laboratory and Oil and Gas Center of Excellence at the University of Tehran. The authors acknowledge Siu on Tung and Tapiwa Mushove at University of Michigan, Ann Arbor for their help in SEM analysis.

Appendix A. Supplementary data

Supplementary data associated with this article can be found, in the online version, at <http://dx.doi.org/10.1016/j.apcatb.2015.06.025>.

References

- [1] C.S. Song, Catal. Today 86 (2003) 211–263.
- [2] J.G. Park, C.H. Ko, K.B. Yi, J.H. Park, S.S. Han, S.H. Cho, J.N. Kim, Appl. Catal. B – Environ. 81 (2008) 244–250.
- [3] P. Baeza, G. Aguilera, G. Vargas, J. Ojeda, P. Araya, Appl. Catal. B – Environ. 111–112 (2012) 133–140.
- [4] A.D. Giuseppe, M. Crucianelli, F.D. Angelis, C. Crestini, R. Saladino, Appl. Catal. B – Environ. 89 (2009) 239–245.
- [5] J. Xiao, Z. Li, B. Liu, Q. Xia, M. Yu, Energy Fuels 22 (2008) 3858–3863.
- [6] C.S. Shalaby, S.K. Saha, X. Ma, C.S. Song, Appl. Catal. B – Environ. 101 (2011) 718–726.
- [7] S. Haji, Y. Zhang, C. Erkey, Appl. Catal. A – Gen. 374 (2010) 1–10.
- [8] A.J. Hernández-Maldonado, F.H. Yang, G. Qi, R.T. Yang, Appl. Catal. B – Environ. 56 (2005) 111–126.
- [9] S.P. Hernandez, D. Fino, N. Russo, Chem. Eng. Sci. 65 (2010) 603–609.
- [10] X. Ma, S. Velu, J.H. Kim, C.S. Song, Appl. Catal. B – Environ. 56 (2005) 137–147.
- [11] C.H. Ko, J.G. Park, J.C. Park, H. Song, S.S. Han, J.N. Kim, Appl. Surf. Sci. 253 (2007) 5864–5867.
- [12] M.V. Landau, M. Herskowitz, R. Agnihotri, J.E. Keggerreis, Ind. Eng. Chem. Res. 47 (2008) 6904–6916.
- [13] A. Boumaza, L. Favaro, J. Lédion, G. Sattonnay, J.B. Brubach, P. Berthet, A.M. Huntz, P. Roy, R. Tétot, J. Solid State Chem. 182 (2009) 1171–1176.
- [14] T.K. Phung, A. Lagazzo, M.Á.R. Crespo, V.S. Escribano, G. Busca, J. Catal. 311 (2014) 102–113.
- [15] B.W. Hoffer, A.D. van Langeveld, J.P. Janssens, R.L.C. Bonné, C.M. Lok, J.A. Moulijn, J. Catal. 192 (2000) 432–440.
- [16] S. Rane, Ø. Borg, J. Yang, E. Rytter, A. Holmen, Appl. Catal. A – Gen. 388 (2010) 160–167.
- [17] Y.H. Kim, E.D. Park, Appl. Catal. B – Environ. 96 (2010) 41–50.
- [18] K. Pattamakomsan, E. Ehret, F. Morfin, P. Gélin, S. Prakash, J.C. Bertolini, J. Panpranot, Y. Jugnet, F.J.C.S. Aires, Catal. Today 164 (2011) 28–33.
- [19] F. Bentaleb, E. Marceau, Micropor. Mesopor. Mat. 156 (2012) 40–44.
- [20] D. Laurenti, B. Phung-Ngoc, C. Roukoss, E. Devers, K. Marchand, L. Massin, L. Lemaitre, C. Legens, A.A. Quoineaud, M. Vrinat, J. Catal. 297 (2013) 165–175.
- [21] K.V.R. Chary, P.V.R. Rao, V.V. Rao, Catal. Commun. 9 (2008) 886–893.
- [22] S.N. Rashkeev, K. Sohlberg, M.V. Glazoff, J. Novak, S.J. Pennycook, S.T. Pantelides, Phys. Rev. B 67 (2003) 115414.
- [23] A. Mansouri, A.A. Khodadadi, Y. Mortazavi, J. Hazard. Mater. 271 (2014) 120–130.
- [24] C. Louis, Z.X. Cheng, M. Che, J. Phys. Chem. 97 (1993) 5703–5712.
- [25] Y.S. Wu, J. Ma, F. Hu, M.C. Li, J. Mater. Sci. Technol. 28 (2012) 572–576.
- [26] M. El Doukkali, A. Iriondo, J.F. Cambra, I. Gandarias, L. Jalowiecki-Duhamel, F. Dumeignil, P.L. Arias, Appl. Catal. A – Gen. 472 (2014) 80–91.
- [27] A. Bazyari, A.A. Khodadadi, N. Hosseinpour, Y. Mortazavi, Fuel Process. Technol. 90 (2009) 1226–1233.
- [28] G. Busca, Catal. Today 226 (2013) 2–13.
- [29] J. Lif, I. Odenbrand, M. Skoglundh, Appl. Catal. A – Gen. 317 (2007) 62–69.
- [30] F.M. Buatista, J.M. Campelo, A. Garcia, D. Luna, J.M. Marinas, J. Catal. 107 (1987) 181–194.
- [31] R. Yang, J. Wu, X. Li, X. Zhang, Z. Zhang, J. Guo, Appl. Catal. A – Gen. 383 (2010) 112–118.
- [32] Y. Nakagawa, H. Nakazawa, H. Watanabe, K. Tomishige, ChemCatChem 4 (2012) 1791–1797.
- [33] G. Zhang, T. Sun, J. Peng, S. Wang, S. Wang, Appl. Catal. A – Gen. 462–463 (2013) 75–81.
- [34] B.M. Vogelaar, A.D. van Langeveld, P.J. Kooyman, C.M. Lok, R.L.C. Bonné, J.A. Moulijn, Catal. Today 163 (2011) 20–26.
- [35] L. He, Y. Huang, A. Wang, Y. Liu, X. Liu, X. Chen, J.J. Delgado, X. Wang, T. Zhang, J. Catal. 298 (2013) 1–9.
- [36] A. Roman, B. Delmon, J. Catal. 30 (1973) 333–342.
- [37] R. Wang, Y. Li, R. Shi, M. Yang, J. Mol. Catal. A – Chem. 344 (2011) 122–127.
- [38] B. Roy, K. Artyushkova, H.N. Pham, L. Li, A.K. Datye, C.A. Leclerc, Int. J. Hydr. Energy 37 (2012) 18815–18826.
- [39] J. Xiao, C. Song, X. Ma, Z. Li, Ind. Eng. Chem. Res. 51 (2012) 3436–3443.
- [40] J.H. Kim, X. Ma, A. Zhou, C. Song, Catal. Today 111 (2006) 74–83.
- [41] F. Subhan, B.S. Liu, Chem. Eng. J. 178 (2011) 69–77.
- [42] M.A. Larrubia, A. Gutiérrez-Alejandre, J. Ramírez, G. Busca, Appl. Catal. A – Gen. 224 (2002) 167–178.
- [43] S. Nair, A.H.M. Shahadat Hussain, B.J. Tatarchuk, Fuel 105 (2013) 695–704.
- [44] X. Ma, M. Sprague, C. Song, Ind. Eng. Chem. Res. 44 (2005) 5768–5775.
- [45] L. Huang, G. Wang, Z. Qin, M. Dong, M. Du, H. Ge, X. Li, Y. Zhao, J. Zhang, T. Hu, J. Wang, Appl. Catal. B – Environ. 106 (2011) 26–38.
- [46] R.R. Lesieur, C. Teeling, J.J. Sangiovanni, L.R. Boedeker, Z.A. Dardas, H. Huang, J. Sun, X. Tang, L.J. Spadaccini, U.S. Patent 6454935 B1 (2002).
- [47] R.R. Lesieur, B.A. Cocolicchio, A.M. Vincitore, U.S. Patent 6726836 B1 (2004).
- [48] A. Samokhalov, E.C. Duin, S. Nair, M. Bowman, Z. Davis, B.J. Tatarchuk, J. Phys. Chem. C 114 (2010) 4075–4085.
- [49] I. Bezverkhyy, A. Ryzhikov, G. Gadacz, J.P. Bellat, Catal. Today 130 (2008) 199–205.
- [50] J.M. Saleh, C. Kemball, M.W. Roberts, Trans. Faraday Soc. 57 (1961) 1771–1780.
- [51] P.J. Mangnus, E.K. Poels, A.D. van Langeveld, J.A. Moulijn, J. Catal. 137 (1992) 92–101.
- [52] S. Dasgupta, P. Gupta, A. Aarti, A.N. Nanoti, M.O. Goswami, E. Garg, Tangstad, B. Ø. Vistad, A. Karlsson, M. Stöcker, Fuel 108 (2013) 184–189.